STREST

D 3.2

DELIVERABLE

PROJECT INFORMATION

Project Title:	**Harmonized approach to stress tests for critical infrastructures against natural hazards**
Acronym:	**STREST**
Project N°:	603389
Call N°:	FP7-ENV-2013-two-stage
Project start:	01 October 2013
Duration:	36 months

DELIVERABLE INFORMATION

Deliverable Title:	**Report on the definition of extreme hazard scenarios for geographically-extended facilities**
Date of issue:	31 March 2015
Work Package:	WP3 – Integrated low probability-high consequence hazard assessment for critical infrastructures
Editor/Author:	Sinan Akkar (BU)
Reviewer:	Laurentiu Danciu (ETHZ)

REVISION: Version 2

SEVENTH FRAMEWORK PROGRAMME

Project Coordinator:	Prof. Domenico Giardini
Institution:	ETH Zürich
e-mail:	giardini@sed.ethz.ch
fax:	+ 41 446331065
telephone:	+ 41 446332610

Abstract

The conventional integral approach is very well established in probabilistic seismic hazard assessment (PSHA). However, Monte-Carlo (MC) simulations may become an efficient and flexible option against conventional PSHA when more complicated factors (e.g., spatial correlation of ground shaking) are involved. Under the framework of the STREST project, the major objective of Task 3.2 is to define hazard measures and extreme event scenarios for geographically extended lifeline systems with emphasis on continuous pipelines. To this end, this report describes the implementation of MC simulation techniques for computing the annual exceedance rates of dynamic ground-motion intensity measures (GMIMs) (e.g., peak ground acceleration-PGA, peak ground velocity-PGV and spectral acceleration-S_a) as well as permanent fault displacement that are of significance for the risk assessment of geographically distributed and extended structures. We use the multi-scale random fields (MSRFs) technique to incorporate spatial correlation and near-fault directivity while generating MC simulations to assess the probabilistic seismic hazard of dynamic GMIMs. Our approach is capable of producing conditional hazard curves as well. The implementation of MC simulations for permanent fault displacement hazard accounts for surface rupture, mapping accuracy and occurrence probabilities of on- and off-fault displacements. We show various parametric case studies to illustrate the potential use of the proposed procedures in the hazard of geographically distributed and extended structural systems. Since permanent fault displacement is the most critical ground-motion intensity measure for design and performance assessment of pipeline systems, the report particularly focuses on the definition of hazard corresponding to rare and extreme event scenarios (low-probability and high-consequence events) for permanent fault displacement hazard.

Keywords: continuous pipelines, Monte Carlo simulations, probabilistic seismic hazard

Acknowledgments

We thank Dr. Mark Petersen and Dr. Rui Chen for explaining the case study in Petersen et al. (2011) and sharing their probabilistic fault displacement hazard assessment codes for the validation of our methodology.

Deliverable Contributors

Boğaziçi University – Kandilli Observatory and Earthquake Research Institute	Sinan Akkar
Boğaziçi University – Kandilli Observatory and Earthquake Research Institute	Yin Cheng
Boğaziçi University – Kandilli Observatory and Earthquake Research Institute	Eren Uçkan
Boğaziçi University – Kandilli Observatory and Earthquake Research Institute	Mustafa Erdik

Table of Contents

List of Figures

List of Tables

1 Introduction

The consideration of site-to-site variation (spatial correlation) in dynamic GMIMs (e.g., PGA, S_a) is important for realistic probabilistic seismic hazard and risk assessment of geographically distributed building portfolios and geographically extended lifeline systems. The interdependency between the GMIMs (cross-correlation) is also important for such structural systems because the vulnerability of some of their components is sensitive to the conditional occurrence of multiple GMIMs. Apart from these two phenomena, the proper amplitude estimations of static (permanent fault displacement) and dynamic GMIMs is crucial for geographically distributed buildings or geographically extended lifelines located in the close proximity to fault segments.

Studies to model spatial correlation (e.g., Boore et al., 2003; Wang and Takada, 2005; Goda and Hong, 2008; Jayaram and Baker, 2009; Esposito and Iervolino, 2011; Goda and Atkinson, 2009), cross-correlation (e.g., Baker and Jayaram, 2008; Bradley, 2011; Bradley, 2012a, 2012b; Cimellaro, 2013; Akkar et al., 2014c; 2014d), combined effects of spatial- and cross-correlation (e.g., Goda and Hong, 2008; Loth and Baker, 2013) as well as near-fault effects for static and dynamic GMIMs (e.g., Stepp et al., 2001; Youngs et al., 2003; Petersen et al., 2011; Somerville, 2003; Tothong et al., 2007; and Shahi and Baker, 2011; Bayless and Somerville, 2013; Chiou and Spudich, 2013; Rowshandel, 2013) are abundant in the literature. There are also several papers showing their implementations by using conventional probabilistic seismic hazard assessment (PSHA; Cornell, 1968) (e.g., Iervolino et al., 2010; Chioccarelli et al., 2012; Shahi and Baker, 2011; Stepp et al., 2001; Youngs et al., 2003; Petersen et al., 2011). Alternative to conventional PSHA, Monte Carlo (MC) simulation techniques have become appealing in probabilistic hazard and risk calculations as they provide some flexibility, transparency and robustness to the consideration of above stated physical models (e.g., Sokolov and Wenzel, 2011a, 2011b; Musson, 1999, 2000; Crowley and Bommer, 2006; Assatourians and Atkinson, 2012; Atkinson and Goda, 2013).

Consideration of spatial correlation for MC-based seismic hazard assessment has been done by generating normally distributed and spatially correlated GMIMs via Cholesky decomposition (e.g., Sokolov and Wenzel, 2011a). The normal sampling of GMIMs uses the mean and standard deviation of the ground-motion prediction equations (GMPEs) that remain constant for the sites (cells) considered in the simulations. This approach may experience some practical difficulties in some cases, for example, while incorporating the forward directivity effects on the sampled GMIMs as narrow-band models opt for modifying the standard deviation of GMPEs depending on the occurrence likelihood of directivity pulse at a site (e.g., Shahi and Baker, 2011).

This report provides the theory and application of MC simulation technique for probabilistic seismic hazard assessment of geographically distributed and extended structural systems. We apply MC simulations together with the multi-scale random fields (MSRFs) approach to account for spatial correlation in estimating joint hazard of dynamic GMIMs. This method is implemented to understand the mechanical behavior of heterogeneous soil medium under different levels of uncertainty (Chen et al., 2012). We propagate its application into PSHA as an alternative to Cholesky decomposition technique. MSRFs can account for spatial

correlation at different precision scales in order to fine-tune the accuracy of hazard curves at the mesh grids of interest. It also permits the modifications to standard deviations at several grid points to account for specific earthquake features such as forward directivity effects. Using these particular properties of MSRFs technique and flexibility provided by MC simulations, we further implemented the near-fault directivity effects on the hazard computations. The MC-based simulations are also implemented to permanent fault displacement hazard by using the model provided in Petersen et al. (2011). To our knowledge, this is the first time that MC-based hazard calculation is used for probabilistic fault displacement hazard assessment. The report first describes the theory of probabilistic hazard assessment for dynamic GMIMs through the application of MC-based MSRFs approach with the inclusion of near-fault effects and conditional hazard. The theoretical part extends to the explanations of how MC simulations are used in the assessment of probabilistic fault displacement hazard. We present several parametric case studies to show the strengths of the proposed procedures for assessing the seismic hazard of geographically distributed building portfolios and geographically extended lifeline systems. The parametric case studies on fault displacement hazard is of particular focus in this report, as the main objective of Deliverable 3.2 is the determination of low-probability-high-consequence hazard levels for continuous pipelines. Such hazard levels are generally referred to as "*perfect storm"* and "*black swan"* in risk analysis and their consideration (e.g., extreme cascading ruptures by adding knowledge from the physics of rupture propagation by dynamic stress; Mignan et al., 2015) would let the owner evaluate the performance of the structural system under critical circumstances.

2 Monte-Carlo based multi-scale random fields for dynamic GMIMs

The multi-scale random fields (MSRFs) hierarchically characterize the randomness of a physical process at different resolution levels. We use this concept together with MC simulation to generate spatially correlated intra-event (site-to-site) residuals by following Chen et al. (2012) who studied the mechanical behavior of heterogeneous soil medium under different levels of uncertainty. The spatially correlated intra-event residuals leads to sampling of spatially correlated GMIMs over the region of interest. The sampled GMIMs can account for near-fault directivity effects depending on the relative location of the site with respect to the fault. Our procedure also considers cross-correlation of sampled primary and secondary GMIMs to assess conditional hazard. The overall MSRFs theory and its implementation are discussed bellow.

We implement two scale levels (coarse-scale and fine-scale) while generating spatially correlated intra-event residuals. Fig. 2.1 illustrates the coarse-scale and fine-scale random fields (coarse-scale and fine-scale cells). The sampled intra-event residuals in a coarse-scale cell are the average of sampled intra-event residuals within the corresponding coarse-scale cell. This relationship is given in Eq. (2.1) where *Z* stands for the sampled intra-event residual. The indices “1” and “2” designate coarse-scale and fine-scale cells, respectively. *n* is the number of fine-scale cells within the coarse-scale cell and *b* represents the index number of the coarse-scale cell.

$$Z_{1,b} = \frac{1}{n}\sum_{i=1}^{n} Z_{2,bi} \tag{2.1}$$

The intra-event residuals are sampled via MC simulation and we make use of the intra-event standard deviation of the GMPE used in the entire process. The intra-event standard deviation accounts for the variability in sampled intra-event residuals. Spatial correlation is considered while sampling the intra-event residuals to mimic the interdependency of generated GMIMs at closely spaced sites (cells) because the waveform radiation patterns are coherent at close sites under a given earthquake. The intra-event residual sampling starts from coarse-scale fields and extend into fine-scale as well as coarse-to-fine scale cells through sequential conditional simulation. The sequential conditional simulation transfers the knowledge of previously sampled intra-event residuals to the next sampled intra-event residual.

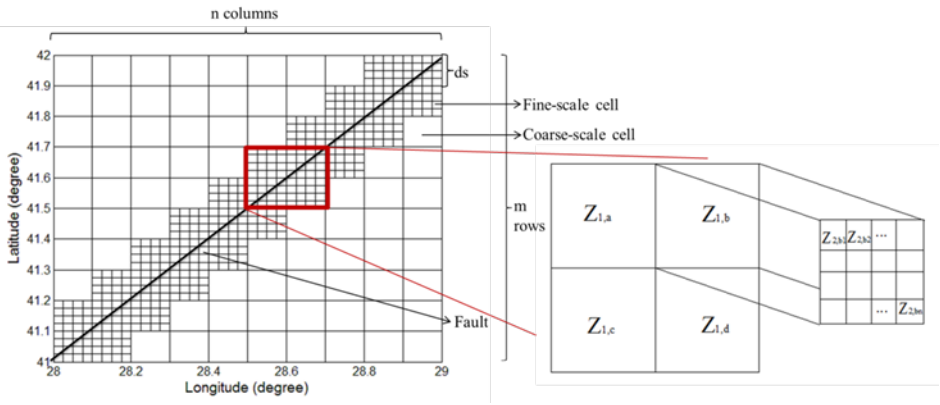

Fig. 2.1 Graphical representation of coarse-scale and fine scale cells in fictitious area. The solid diagonal line is the fault. The area is divided into m×n squared coarse-scale cells. Some of the coarse-scale cells are further refined into ds×ds fine scale cells. Note that these coarse-scale cells are located in the vicinity of fault segment and they are divided into finer scale cells to better capture the near-fault directivity effects. The right panel is the close-up view of 4 coarse scale cells located in the vicinity of the fault and, for illustration purposes, we show one of these coarse scale cells refined into 6×6 fine-scale cells

Although MC-based intra-event residual sampling starts at coarse-scale level, the sampling distributions of coarse-scale and fine-scale cells are directly related to each other. The intra-event residual distribution at fine-scale level is normal with zero mean and standard deviation σ_{Z2}. Note that σ_{Z2} is the intra-event standard deviation of the pertaining GMPE used in the calculations. Eq. (2.1) leads to the below expressions to compute the mean (μ_{Z1}) and standard deviation (σ_{Z1}) of normally distributed intra-event residuals for coarse-scale cells.

$$\mu_{Z1} = E(Z_1) = E(\frac{1}{n}\sum_{i=1}^{n} Z_{2i}) = \frac{1}{n}E(\sum_{i=1}^{n} Z_{2i}) = \frac{1}{n}\sum_{i=1}^{n} E[Z_{2i}] = 0 \tag{2.2}$$

$$\sigma_{Z1}^2 = E[Z_1^2] - E[Z_1]^2 = E[Z_1^2] - 0 = \frac{1}{n^2}\sum_{i=1}^{n}\sum_{j=1}^{n} \rho_{Z2i,Z2j} \cdot \sigma_{Z2i} \cdot \sigma_{Z2j} \tag{2.3}$$

In Eq. (2.3), $\rho_{Z2i,Z2j}$ is the spatial correlation coefficient between two fine-scale cells that is controlled by the separation distance between them. As discussed in the introductory section, there is a handful of spatial correlation models in the literature for calculating $\rho_{Z2i,Z2j}$ (e.g., Goda and Hong, 2008). σ_{Z2i} and σ_{Z2j} are the intra-event residual standard deviations of the *ith* and *jth* fine-scale cells, respectively. *Z* is the sampled intra-event residual, *n* is the number of fine-scale cells in the corresponding coarse-scale cell and indices *1* and *2* indicate coarse-scale and fine-scale cells, respectively. *E* denotes the expected value operator. The spatial correlation coefficient between two fine-scale cells, $\rho_{Z2i,Z2j}$, is used to derive spatial correlation coefficients for coarse-to-coarse scale and coarse-to-fine scale cells. These expressions are given in Eq. (2.4) and Eq. (2.5) and are used to sample intra-event residuals by sequential conditional simulation.

$$\rho_{Z1a,Z1b} = \frac{\mathrm{cov}[Z_{1a}, Z_{1b}]}{\sigma_{Z1a}\sigma_{Z1b}} = \frac{\mathrm{cov}[1/n\sum_{i=1}^{n} Z_{2ai}, 1/n\sum_{k=1}^{n} Z_{2bk}]}{\sqrt{1/n^2\sum_{i=1}^{n}\sum_{j=1}^{n}\rho_{Z2ai,Z2aj}\cdot\sigma_{Z2ai}\cdot\sigma_{Z2aj}}\sqrt{1/n^2\sum_{i=1}^{n}\sum_{j=1}^{n}\rho_{Z2bi,Z2bj}\cdot\sigma_{Z2bi}\cdot\sigma_{Z2bj}}} = \frac{\sum_{i=1}^{n}\sum_{k=1}^{n}\mathrm{cov}(Z_{2bi}, Z_{2ak})}{\sqrt{\sum_{i=1}^{n}\sum_{j=1}^{n}\rho_{Z2ai,Z2aj}\cdot\sigma_{Z2ai}\cdot\sigma_{Z2aj}}\cdot\sqrt{\sum_{i=1}^{n}\sum_{j=1}^{n}\rho_{Z2bi,Z2bj}\cdot\sigma_{Z2bi}\cdot\sigma_{Z2bj}}} = \frac{\sum_{i=1}^{n}\sum_{k=1}^{n}\rho_{z_{2ai},z_{2bk}}\cdot\sigma_{z_{2ai}}\cdot\sigma_{z_{2bk}}}{\sqrt{\sum_{i=1}^{n}\sum_{j=1}^{n}\rho_{Z2ai,Z2aj}\cdot\sigma_{Z2ai}\cdot\sigma_{Z2aj}}\cdot\sqrt{\sum_{i=1}^{n}\sum_{j=1}^{n}\rho_{Z2bi,Z2bj}\cdot\sigma_{Z2bi}\cdot\sigma_{Z2bj}}} \quad (2.4)$$

$$\rho_{Z2,Z1a} = \frac{\mathrm{cov}[Z_2, Z_{1a}]}{\sigma_{Z2}\sigma_{Z1a}} = \frac{\mathrm{cov}[Z_2, 1/n\sum_{i=1}^{n} Z_{2ai}]}{\sigma_{Z2}\sqrt{1/n^2\sum_{i=1}^{n}\sum_{j=1}^{n}\rho_{Z2ai,Z2aj}\cdot\sigma_{Z2ai}\cdot\sigma_{Z2aj}}} = \frac{\sum_{i=1}^{n}\mathrm{cov}(Z_2, Z_{2ai})}{\sigma_{Z2}\sqrt{\sum_{i=1}^{n}\sum_{j=1}^{n}\rho_{Z2ai,Z2aj}\cdot\sigma_{Z2ai}\cdot\sigma_{Z2aj}}} = \frac{\sum_{k=1}^{n}\rho_{Z2,Z2ai}\cdot\sigma_{Z2}\cdot\sigma_{Z2ai}}{\sigma_{Z2}\sqrt{\sum_{i=1}^{n}\sum_{j=1}^{n}\rho_{Z2ai,Z2aj}\cdot\sigma_{Z2ai}\cdot\sigma_{Z2aj}}} = \frac{\sum_{k=1}^{n}\rho_{Z2,Z2ai}\cdot\sigma_{Z2ai}}{\sqrt{\sum_{i=1}^{n}\sum_{j=1}^{n}\rho_{Z2ai,Z2aj}\cdot\sigma_{Z2ai}\cdot\sigma_{Z2aj}}} \quad (2.5)$$

In the above expressions, $\rho_{Z1a,Z1b}$ and $\rho_{Z2,Z1a}$ refer to coarse-to-coarse scale and fine-to-coarse scale correlation coefficients, respectively. The parameters *a* and *b* indicate the index numbers of coarse-scale cells. Eq. (2.6) shows the joint distribution expression used in the spatially correlated intra-event sampling by conditional sequential simulation.

$$\begin{bmatrix} Z_n \\ \boldsymbol{Z}_p \end{bmatrix} \sim N(\boldsymbol{\mu}, \boldsymbol{\Sigma}) = N\left(\begin{bmatrix} 0 \\ \mathbf{0} \end{bmatrix}, \begin{bmatrix} \sigma_n^2 & \boldsymbol{\Sigma}_{np} \\ \boldsymbol{\Sigma}_{pn} & \boldsymbol{\Sigma}_{pp} \end{bmatrix}\right) \quad (2.6)$$

The subscripts *n* and *p* describe the “next” and “previously” generated intra-event residuals, respectively in the above equation. The vector $\boldsymbol{Z}=[Z_n\ \boldsymbol{Z_p}]$ follows a joint normal distribution with a vector of zero mean and covariance matrix, ∑. The distribution of the next sampled data (Z_n) is a univariate normal distribution conditioned on the previously sampled realizations ($\boldsymbol{Z_p}$) that is given in Eq. (2.7) and Eq. (2.8).

$$\left[Z_n \mid \boldsymbol{Z}_p = \boldsymbol{z}\right] \sim N\left(\boldsymbol{\Sigma}_{np}\cdot\boldsymbol{\Sigma}_{pp}^{-1}\cdot\boldsymbol{z}, \sigma^2 - \boldsymbol{\Sigma}_{np}\cdot\boldsymbol{\Sigma}_{pp}^{-1}\cdot\boldsymbol{\Sigma}_{pn}\right) \quad (2.7)$$

$$\mathrm{COV}\left[Z_i, Z_j\right] = \rho_{Z_i,Z_j}\cdot\sigma_{Z_i}\cdot\sigma_{Z_j} \quad (2.8)$$

While sampling the intra-event residuals of coarse-scale cells, the covariance matrix (∑) given in Eq. (2.8) considers the spatial correlation between two coarse-scale cells as shown in Eq. (2.4) *equation reference goes here*. The corresponding intra-event standard deviations σ_{Zi} and σ_{Zj} can be calculated from Eq. (2.3). If the intra-event residual sampling is for fine-scale cells, the covariance matrix should consider the spatial correlation between two

fine-scale cells ($\rho_{Z2i,Z2j}$), two coarse-scale cells (Eq. (2.4)) as well as one coarse-scale cell and one fine-scale cell (Eq. (2.5)). Accordingly, the intra-event standard deviations in Eq. (2.8) would correspond to one of these three cases for the intra-event residual sampling of fine scale cells. These concepts are further clarified in the following paragraphs.

Fig. 2.2 illustrates the generation of intra-event residuals at coarse-scale level. The area of interest is divided into a number of coarse-scale cells and indexed from left-to-right and bottom-to-top as given in the leftmost side of Fig. 2.2. The sequential indices are resorted in a random manner to generate a new (random) sequence of indices (middle part in Fig. 2.2). Following the new order of randomized coarse-scale cells, the intra-event residuals are generated for each cell at the coarse-scale level by using the sequential conditional simulation procedure as summarized in Eq. (2.6), Eq. (2.7) and Eq. (2.8). The intra-event residual of first coarse-scale cell (Z_3 in the illustrative example as given in the rightmost part in Fig. 2.2) is sampled as a univariate normal distribution. The intra-event residual of coarse-scale cell following the first one (Z_5 in Fig. 2.2) is sampled by using the sampled intra-event residual of first coarse-cell (Z_3). In essence, while generating the intra-event residual of the "next" cell, Z_n, the previously generated intra-event residuals become the entries in $\boldsymbol{Z_p}$. The procedure is recursively repeated until all the intra-event residuals in the coarse-scale cells are sampled.

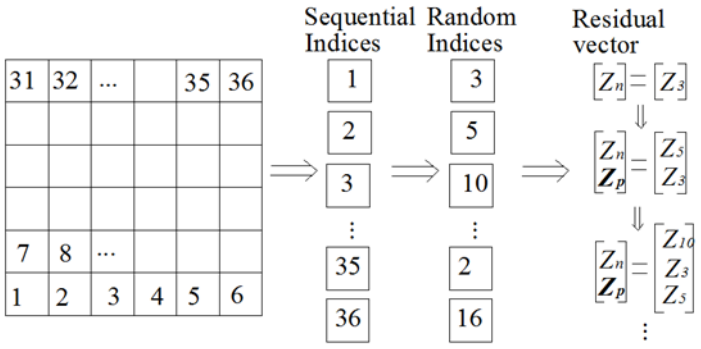

Fig. 2.2 Illustrative example for intra-event residual sampling at coarse-scale level

The intra-event residual simulation of coarse-scale cells is followed by a similar set of simulations at fine-scale level. This process is illustrated in Fig. 2.3 as the continuation of the example case in Fig. 2.2. Although the entire coarse-scale cells can be refined into fine-scale cells to generate the intra-event residuals at the fine-scale level, this process may bring computational burden depending on the size of the area of interest, the number of coarse-scale cells as well as the level of mesh gridding at the fine-scale level (i.e., the number of fine-scale cells in coarse-scale cells). We prefer pre-defining the coarse-scale cells to be refined into fine-scale cells in our procedure. The level of precision for observing the near-fault effects on hazard computations or requirements to be fulfilled in the development of conditional hazard curves can play a role on the number of pre-defined coarse-scale cells for fine-scale mesh gridding. The order of coarse-scale cells to be refined into fine-scale cells should follow the random indexing used while generating the intra-event residuals of coarse-scale cells. In the follow-up example given in Fig. 2.3, the coarse-scale cells indexed as #2 and #3 are chosen to be refined into fine-scale cells (Fig. 2.3.a). Note that the random coarse-scale cell indexing given in Fig. 2.2 indicates that conditional sequential simulation for fine-scale cells should start from coarse-scale cell #3 and should be

followed by refining the coarse-scale cell #2. Similar to the indexing technique given in Fig. 2.2, the fine-scale cells in the #2 and #3 coarse-scale cells are numbered from left-to-right and from bottom-to-top as shown in Fig. 2.3.a. For this illustrative case, each coarse-scale cell is mesh gridded into 2×2 fine-scale cells. The fine-scale cell indices are then randomized (leftmost part in Fig. 2.3.b) to start sequential conditional simulation. For example, the randomized indices of fine-scale cells in the #3 coarse-scale cell are [4, 2, 3, 1]. As presented in the illustrative case in Fig. 2.3, the intra-event residual of the #4 fine-scale cell in the #3 coarse-scale cell ($Z_{3,4}$) is sampled by using Eq. (2.6) to Eq. (2.8) where $\boldsymbol{Z_p}$ contains all previously sampled coarse-scale cell intra-event residuals. The intra-event residual sampling $Z_{3,2}$, $Z_{3,3}$ and $Z_{3,1}$ is followed after $Z_{3,4}$. After each realization, the corresponding sampled intra-event residual is an entry in $\boldsymbol{Z_p}$. Upon the sampling of all intra-event residuals in the fine-scale cells of a coarse-scale cell (e.g., #3 coarse-scale cell in Fig. 2.3), it is removed from the previously sampled realizations vector, $\boldsymbol{Z_p}$. The entire process is repeated until the sampling of all intra-event residuals at fine-scale level is finished in the pre-defined coarse-scale random fields. The following section extends our approach to include near-fault forward directivity effects on the spatially correlated dynamic GMIMs generated via MC-based MSRFs approach.

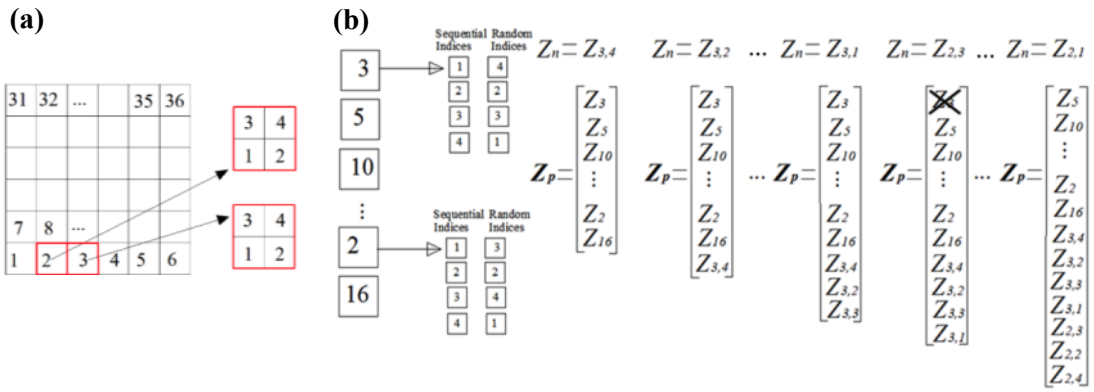

Fig. 2.3 Generation of intra-event residuals for fine-scale cells: (a) pre-selected coarse-scale cells for refining into fine-scale cells (designated by red boxes) and numbering of fine-scale cells in these coarse-scale cells, (b) sequential conditional simulation process

2.1 NEAR-FAULT DIRECTIVITY EFFECTS

Pulse-like ground motions due to superposed propagation velocities of rupture and seismic waves (forward directivity) induce significantly large demands on structures. Such specific ground motions are generally observed at the near-fault sites. Most of the conventional GMPEs do not model near-fault forward directivity so seismic hazard assessment via conventional ground-motion characterization may fail to estimate the near-fault ground-motion amplitudes for future earthquakes. We implemented the near-fault directivity model of Shahi and Baker (2011) to account for the likely change of ground-motion amplitudes in the vicinity of faults. The Shahi and Baker model predicts the probability of pulse-like ground motions occurring at a site by considering the orientations of induced seismic waveforms relative to the strike of the fault. It amplifies the amplitudes of spectral ordinates in the vicinity

of pulse period, T_p, by empirically calibrating the median and standard deviations of ground-motion estimates from conventional GMPEs. The reader is referred to Shahi and Baker (2011) for the details of the model.

Fig. 2.4 shows the overall algorithm for incorporating the near-fault directivity effects to the spatially correlated GMIMs generated via MSRFs approach. In essence, we modify the intra-event standard deviation of the conventional GMPE to sample the spatially correlated intra-event residuals for sites (coarse and fine-scale cells) located in the near-fault region. Considering T_p, we also modify the median estimates of GMIMs for these sites obtained from the conventional GMPE. As indicated in the previous paragraph, these modifications are based on the Shahi and Baker (2011) model.

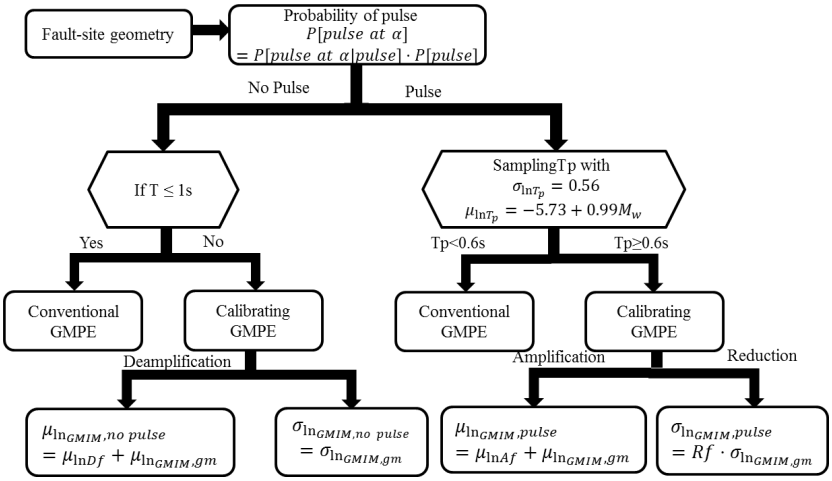

Fig. 2.4 Algorithm for considering near-fault forward directivity effects on the spatially correlated GMIMs generated from MSRFs approach. $\mu_{lnGMIM,pulse}$ is the calibrated mean GMIM in logarithmic space due to pulse-like ground motions (forward directivity). μ_{lnAF} is the logarithmic calibration factor for forward directivity effects and $\mu_{lnGMIM,gm}$ is the mean GMIM in logarithmic space computed from conventional GMPE. In a similar manner, $\sigma_{lnGMIM,pulse}$ and $\sigma_{lnGMIM,gm}$ are the calibrated and original standard deviations of conventional GMPE, respectively. *Rf* is the calibration factor for standard deviation for forward directivity effects. For non-pulse case, $\mu_{lnGMIM,nonpulse}$ is the calibrated mean GMIM in logarithmic space due to nonpulse-like ground motions. μ_{lnAF} and $\sigma_{lnGMIM,nonpulse}$ are the logarithmic calibration factor and standard deviation of GMPE for backward directivity effects, respectively

For each realization of MC simulations (i.e., for each scenario event), we determine the probability of observing a pulse at a certain orientation α [P(pulse at α|pulse)] for near-fault sites (cells) by considering their relative locations with respect to the fault strike. We sample this probability with binomial distribution. If the forward directivity is more likely to occur (Pulse case), we sample T_p assuming log-normal distribution. The value of sampled T_p leads to the calibration of median ground motion and associated standard deviation of conventional GMPE to generate spatially correlated random fields. The Shahi and Baker (2011) model disregards the calibration of median ground motion and associated standard deviation if T_p < 0.6s. If the backward directivity is more dominant (No Pulse case), then depending on the spectral period (T) of GMIM, this model either uses the median ground-motion estimates and standard deviation of conventional GMPE (T ≤ 1.0s case) or modifies

these parameters. The calibrated standard deviations and median ground-motion estimates are used for generating spatially correlated GMIMs with forward (or backward) directivity effects at coarse- and fine-scale levels.

The Shahi and Baker model provides calibration factors for the total standard deviation of a conventional GMPE that can be used for generating total residuals. Since our MSRFs approach requires intra-event standard deviation ($\sigma_{\varepsilon,gm}$) to sample intra-event residuals, we modify the calibration factor proposed in Shahi and Baker as given in Eq. (2.9) and Eq. (2.10). We assume that the inter-event standard deviation ($\sigma_{\eta,gm}$) does not change for any given simulated scenario earthquake. This assumption is rational as inter-event standard deviation is constant for a specific earthquake. The modified calibration factor is indicated as $Rf_{\varepsilon,\,pulse}$ in the derivations and replaces R_f while considering the near-fault directivity effects in our MSRFs approach. Note that $\sigma_{\eta,gm}$ and $\sigma_{\eta,pulse}$ are equal to each other in the derivations under constant inter-event standard deviation assumption.

$$\begin{aligned} Rf^2 &= \frac{\sigma^2_{t,pulse}}{\sigma^2_{t,gm}} = \frac{\sigma^2_{\varepsilon,pulse}+\sigma^2_{\eta,pulse}}{\sigma^2_{\varepsilon,gm}+\sigma^2_{\eta,gm}} \\ &= \frac{\sigma^2_{\varepsilon,pulse}/\sigma^2_{\varepsilon,gm}+\sigma^2_{\eta,pulse}/\sigma^2_{\varepsilon,gm}}{1+\sigma^2_{\eta,gm}/\sigma^2_{\varepsilon,gm}} \\ &= \frac{Rf^2_{\varepsilon,pulse}+\sigma^2_{\eta,pulse}/\sigma^2_{\varepsilon,gm}}{1+\sigma^2_{\eta,gm}/\sigma^2_{\varepsilon,gm}} \\ &= \frac{Rf^2_{\varepsilon,pulse}+\sigma^2_{\eta,gm}/\sigma^2_{\varepsilon,gm}}{1+\sigma^2_{\eta,gm}/\sigma^2_{\varepsilon,gm}} \end{aligned} \tag{2.9}$$

$$\begin{aligned} &\Rightarrow Rf^2_{\varepsilon,pulse} = (1+\sigma^2_{\eta,gm}/\sigma^2_{\varepsilon,gm})\cdot Rf^2 - \sigma^2_{\eta,gm}/\sigma^2_{\varepsilon,gm} \\ &\Rightarrow Rf_{\varepsilon,pulse} = \sqrt{(1+\sigma^2_{\eta,gm}/\sigma^2_{\varepsilon,gm})\cdot Rf^2 - \sigma^2_{\eta,gm}/\sigma^2_{\varepsilon,gm}} \end{aligned} \tag{2.10}$$

The spatial correlation expression, $\rho_{\eta,gm}$, (Wesson and Perkins 2001; Sokolov Wenzel 2011a) in Eq. (2.11) can be used together with Eq. (2.10) to express $Rf_{\varepsilon,\,pulse}$ as given in Eq. (2.12).

$$\rho_{\eta,gm} = \frac{\sigma^2_{\eta,gm}}{\sigma^2_{\varepsilon,gm}+\sigma^2_{\eta,gm}} \tag{2.11}$$

$$Rf_{\varepsilon,pulse} = \sqrt{\frac{1}{1-\rho_{\eta,gm}}(Rf^2-\rho_{\eta,gm})} \tag{2.12}$$

2.2 DEVELOPMENT OF HAZARD CURVES FROM MC-BASED MSRFS APPROACH

This section describes the procedure of estimating the hazard curves that consists of several steps. We first generate a suite of synthetic earthquake catalogs for a given fault located in the area of interest. The synthetic catalogs are based on a specific earthquake recurrence

model that represents the temporal distribution of seismic activity in the considered fault for a certain catalog period. In essence, simulating a suite of synthetic earthquake catalogs having magnitude frequency distributions similar to the one dictated by the earthquake recurrence model covers a long time span to sufficiently address the low annual exceedance rates of earthquakes originating from the considered fault. This approach has been used by Musson (2000) and Assatourias and Atkinson (2013) in MC-based PSHA. Musson (2000) indicated that a suite of 1000 synthetic catalogs, each spanning a 100-year time interval (i.e., a total duration of 100,000 years) would yield reliable estimates of GMIMs for annual exceedance rates of 10^{-3}. When the total catalog duration is extended to 1,000,000 years (i.e., 10000 synthetic catalog, each covering 100-year period), the accurate annual exceedance rates for GMIMs become 10^{-4}. Similar findings are also published by Assatourias and Atkinson (2013) as well as Crowley and Bommer (2006). The latter paper considers all stochastic events in a single earthquake catalog with a very long time period.

Our synthetic catalog simulations assume a Poissonian process for earthquake occurrence. The earthquakes generated in each artificial catalog are assumed to occur randomly on the fault with a uniform distribution along the fault strike and within the seismogenic depth. For each scenario event (a rupture on the fault) in the artificial earthquake catalogs, we implement the MSRFs approach to sample spatially correlated intra-event residuals at coarse- and fine-scale levels. The intra-event residuals are sampled at the centers of coarse-scale and fine-scale cells and consider the near-fault directivity effects depending on the relative location of the site (cell) with respect to fault geometry. We obtain the total residual at each cell by considering the contribution of inter-event residual specific to the scenario event. The inter-event residuals are computed from the inter-event standard deviation of the GMPE used in the entire process. They are sampled as normal varieties in our procedure. The logarithmic mean (median) predictions of GMIM that are computed at the centers of coarse-scale and fine-scale cells are superposed with the total residuals to obtain the spatially correlated GMIM distribution within the entire random field. As in the case of intra-event residual sampling, the median GMIM predictions are modified for near-fault directivity effects depending on the site and fault locations at coarse- and fine-scale levels.

The entire procedure described in the above paragraph is itemized in the following steps:

1. Define the area of interest together with the fault segment that affects the seismicity in the entire area. Subdivide the area into coarse-scale and fine-scale cells with sufficient resolution to compute accurate hazard results. The decision on refining coarse-scale cells into fine-scale cells depend on many factors such as addressing the near-fault directivity effects in the vicinity of fault segment.
2. Chose a GMPE that is suitable for the tectonic environment as well as the seismicity in the area of interest. Eq. (2.13) shows the essential components of a GMPE that are of relevance to our discussions.

$$\ln\left(GMIM_{i,j}\right) = f\left(M_i, R_{i,j}, \theta\right) + \eta_i + \varepsilon_{i,j}; \qquad i = 1,\ldots m,\ j = 1,\ldots n \tag{2.13}$$

   The first term on the left-hand-side predicts the logarithmic mean of the $GMIM_{i,j}$ of interest for the *ith* earthquake and *jth* site (designated as $\mu_{lnGMIM,gm}$ in the previous discussions). M_i and $R_{i,j}$ are the magnitude and source-to-site distance terms of the *ith* earthquake and the *jth* site (cell). The vector θ contains other seismological estimator parameters to define, for example, site conditions at the *jth* site and style-of-faulting specific to the *ith* earthquake. The random varieties η_i and $\varepsilon_{i,j}$ represent the intra-event

and inter-event variability in the predicted $GMIM_{i,j}$, respectively. They are normally distributed with inter-event ($\sigma_{e,gm}$) and intra-event ($\sigma_{\varepsilon,gm}$) standard deviations. Note that *m* and *n* in Eq. (2.13), represent the total number of simulations and sites (cells) at the coarse-scale and fine-scale levels, respectively. The total number of simulations is related to the number of earthquakes in the artificially generated earthquake catalogs.

3. Generate a suite of earthquake catalogs by following the properties of earthquake recurrence specific to the fault. The number of earthquake catalogs should be sufficient enough to consider the occurrence of rare events (low annual exceedance rates) for proper temporal distribution of earthquakes.
4. For scenario event *i*, sample spatially correlated $\varepsilon_{i,j}$ using the MSRFs approach. Make necessary calibrations for near-fault directivity effects at coarse-scale and fine-scale levels whenever necessary.
5. For scenario event *i*, compute the logarithmic mean of $GMIM_{i,j}$ ($\mu_{lnGMIM,gm}$) at coarse-scale and fine-scale levels. Make necessary calibrations for near-fault directivity effects (i.e., modify $GMIM_{i,j}$ either for $\mu_{lnGMIM,pulse}$ or $\mu_{lnGMIM,nonpulse}$) depending on location of the site with respect to fault, T_p and spectral period (T) of $GMIM_{i,j}$.
6. For scenario event *i*, compute η_i.
7. Combine the spatially correlated $\varepsilon_{i,j}$, $GMIM_{i,j}$ and η_i using Eq. (2.13). The product is the spatially correlated $GMIM_{i,j}$ in the logarithmic domain at coarse- and fine-scale levels.
8. Repeat steps 4 to 7 for the simulated suite of earthquake catalogs and compute the hazard curves for the cells (sites) at coarse- and fine-scale levels from Eq. (2.14).

$$\lambda_j\left(GMIM \geq GMIM_0\right) = \frac{total\ number\ of\ GMIM \geq GMIM_0\ at\ site\ j}{total\ number\ of\ simulated\ earthquake\ catalogs \times catalog\ period} \tag{2.14}$$

In Eq. (2.14), $\lambda_j(GMIM \geq GMIM_0)$ is the mean annual rate of GMIM of interest exceeding a threshold level $GMIM_0$ for cell *j*. Computation of $\lambda_j(GMIM \geq GMIM_0)$ for a range of $GMIM_0$ will yield the hazard curve at cell *j*. We note that the computation of hazard curves by MC-based MSRFs approach is described by considering a single fault source. If the area of interest is exposed to *k* multiple faults, this procedure is repeated for the other faults. The mean annul exceedance rates computed from all sources are then summed up to obtain the final mean annual exceedance rate at cell *j*.

$$\lambda_j\left(GMIM \geq GMIM_0\right) = \sum_{l=1}^{k} \lambda_{l,j}\left(GMIM \geq GMIM_0\right) \tag{2.15}$$

2.3 COMPUTATION OF CONDITIONAL HAZARD

The discussions in the previous sections describe the theory and implementation of the MC-based MSRFs approach for the seismic hazard assessment of a single GMIM. The conditional seismic hazard assessment, however, is sometimes more critical for a geographically distributed structural portfolio and geographically extended infrastructures because the seismic performance of some of their components require the consideration of multiple GMIMs. The conditional hazard assesses the exceedance rate of the secondary

GMIMs conditioned on the occurrence of primary GMIM. The secondary GMIMs can be either single or multiple. In case there are multiple secondary GMIMs, they are called as first-secondary GMIM, second-secondary GMIM and so forth. The primary and secondary GMIMs are related to each other by cross-correlation coefficients, $\rho_{IMi,IMj}$ (e.g. Akkar et al., 2014c; 2014d; Baker and Jayaram, 2008).

The conventional conditional hazard assessment cross-correlates each secondary GMIM with the primary GMIM to compute the conditional exceedance rate of secondary GMIMs (Iervolino et al., 2010). The proposed procedure in this paper establishes a different structure: each secondary GMIM is cross-correlated with the primary and previously generated secondary GMIMs for the conditional exceedance rate of the secondary GMIMs. This way the interdependence of primary and secondary GMIMs is more realistically mapped on to the conditional exceedance rates. The procedure does not change for the primary GMIM. We generate the spatially correlated intra-event residuals and sum them up with the independently sampled inter-event residuals to obtain the total residual distribution at coarse- and fine-scale levels for the entire earthquake scenarios of the simulated earthquake catalogs. The total residual sampling of secondary GMIMs is based on the total residual distribution of the primary GMIM and they are generated via sequential conditional simulation. The total residuals of the primary and secondary GMIMs have joint multivariate normal distribution as described in Eq. (2.16) and Eq. (2.17).

$$\begin{bmatrix} Z_{IMn} \\ \boldsymbol{Z}_{IMp} \end{bmatrix} \sim N\left(\boldsymbol{\mu}, \boldsymbol{\Sigma}\right) = N\left(\begin{bmatrix} 0 \\ \boldsymbol{0} \end{bmatrix}, \begin{bmatrix} \sigma_{IMn}^2 & \boldsymbol{\Sigma}_{IMnp} \\ \boldsymbol{\Sigma}_{IMpn} & \boldsymbol{\Sigma}_{IMpp} \end{bmatrix}\right) \tag{2.16}$$

$$\mathrm{COV}\left[Z_{IMi}, Z_{IMj}\right] \sim \rho_{Z_{IMi},Z_{IMj}} \cdot \sigma_{Z_{IMi}} \cdot \sigma_{Z_{IMj}} \tag{2.17}$$

Eq.(2.16) and Eq. (2.17) have a format similar to Eq. (2.6) and Eq. (2.8), respectively. Z_{IMn} refers to the next generated total residual of secondary GMIM whereas $\boldsymbol{Z_{IMp}}$ is the vector of previously generated primary and secondary GMIMs. In a similar manner, σ_{IMn} is the total standard deviation of the next generated secondary GMIM and $\sum_{\boldsymbol{IMnp}}$ as well as $\sum_{IMpn}$ are the covariance vectors of the next and previous GMIMs. The covariance matrix of the previously generated GMIMs is designated as $\sum_{\boldsymbol{IMpp}}$. Note that the covariance terms in Eq. (2.16) contain the previously generated primary and secondary GMIMs as the proposed approach accounts for the interdependency between these varieties. The covariance relationship to be used between the secondary and primary, primary and primary as well as secondary and secondary GMIMs, are given in Eq. (2.17). In this expression, $\rho_{IMi,IMj}$ is the cross-correlation coefficient between GMIM_i and GMIM_j where they can be primary and secondary, both secondary or both primary GMIMs. σ_{ZIMi} and σ_{ZIMi} refer to the corresponding total standard deviations. As explained in the previous sections the standard deviation information comes from the GMPE used in the overall process. The total residual distribution can further be expressed as a univariate normal distribution for the next generated GMIM as given in Eq. (2.18), which is analogous to Eq. (2.7) used in the inter-event residual sampling of primary GMIM.

$$\left[Z_{IMn} \mid \boldsymbol{Z}_{IMp} = z\right] \sim N\left(\boldsymbol{\Sigma}_{IMnp} \cdot \boldsymbol{\Sigma}_{IMpp}^{-1} \cdot z, \sigma_{IMn}{}^2 - \boldsymbol{\Sigma}_{IMnp} \cdot \boldsymbol{\Sigma}_{IMpp}^{-1} \cdot \boldsymbol{\Sigma}_{IMpn}\right) \tag{2.18}$$

In Eq. (2.18) $\boldsymbol{Z_{IMp}}$ is the total residual realizations of the previous GMIMs. Note that we describe the proposed procedure to sample cross-correlated total residuals. If the considered GMPE provides information about the cross-correlation models of intra- and

inter-event residuals separately, it can be modified to sample the cross-correlated intra- and inter-event residuals simultaneously to obtain the hazard rate of secondary GMIMs conditioned on the primary GMIM.

In essence, our procedure for conditional hazard assessment uses the previously generated primary GMIM to sample the total residuals of secondary GMIMs. If there is a second-secondary GMIM, its total residuals are sampled by the cross-correlations of primary, first-secondary and second-secondary GMIMs. This process continues for the entire set of secondary GMIMs. The conditional hazard of each secondary GMIM is then developed by following the conventional approach given in Eq. (2.14). If there is one secondary GMIM, the normal distribution of total residuals of the secondary GMIM will have the following mean ($\mu_{IM2|IM1}$) and standard deviation ($\sigma_{IM2|IM1}$):

In Eq. (2.19), ε is the previously sampled total residual of primary GMIM and is the cross-correlation coefficient between the primary and secondary GMIMs. Fig. 2.5 illustrates this specific case to develop the hazard curve of the secondary GMIM conditioned on the primary GMIM for each cell (site).

$$\mu_{IM2|IM1} = \rho_{IM1,IM2}\sigma_{IM2}\frac{\varepsilon}{\sigma_{IM1}} \tag{2.19}$$

$$\sigma_{IM2|IM1} = \sigma_{IM2}\sqrt{1-\rho^2_{IM1,IM2}} \tag{2.20}$$

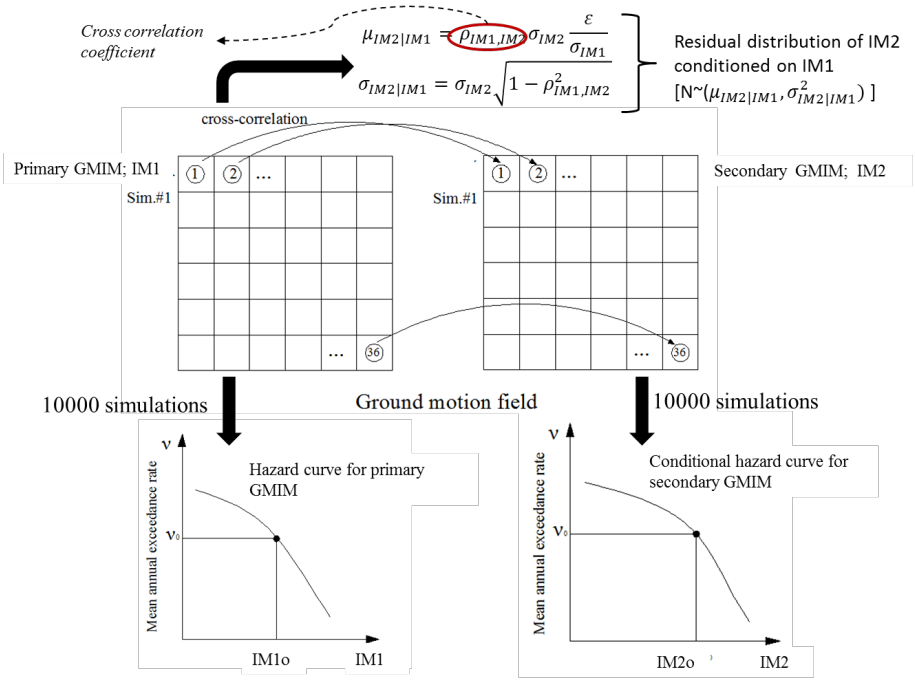

Fig. 2.5 Graphical illustration of conditional hazard assessment for a single secondary GMIM

3 Monte-Carlo based hazard for permanent fault displacement

Geographically distributed and extended systems (e.g., gas, water, oil pipelines, highway networks, large span bridges or large building stocks covering a wide geographical area) can be exposed to severe damage if the faults crossing their footprints rupture at the surface leave permanent deformations. The permanent fault displacements are generally estimated deterministically from empirical surface rupture vs. magnitude relationships (e.g., Wells and Coppersmith, 1994). Inspired from conventional PSHA, Youngs et al. (2003) conducted the first pioneering study for assessing probabilistic fault displacement hazard (PFDHA) to expresses the annual exceedance rates of fault displacements at different thresholds. This approach is improved by Petersen et al. (2011) for strike-slip faults by including the mapping accuracy and complexity of the fault trace. Petersen et al. (2011) model the likely occurrence of on-fault (D) and off-fault (d) displacements where the former displacement occurs on the major ruptured fault and the latter displacement typically represents discontinuous shear-failures at locations far from the principal fault.

The ruptured fault segment and site geometry used in the Petersen et al. (2011) model are presented in Fig. 3.1. The site is represented as a square cell having a dimension of z and x, y denote the coordinates of the center of the site. r is the perpendicular distance from the rupture length, L. l denotes the distance measured from the nearest point on the rupture to the closest end of the rupture whereas s is the distance from the end of the rupture to the end of the fault. The dashed lines in Fig. 3.1 represent the potential deviations in the rupture from the mapped fault due to mapping inaccuracy and complexity of the main fault trace. The rupture deviations from the mapped fault trace can be assumed as single or multiple deviations.

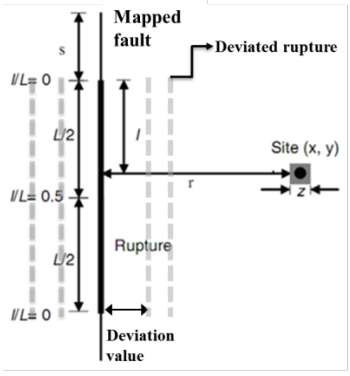

Fig. 3.1 Ruptured fault and site geometry in Petersen et al. (2011) for their proposed PFDHA model for strike-slip events

The annual exceedance rate of on-fault displacement $\gamma(D \geq D_0)$ is considered by integrating different probabilities in Petersen et al. (2011). These probabilistic terms include (1) the uncertainty in rupture location due to random variation of rupture along the fault as well as the fault complexity and mapping inaccuracy, $f(r)$; (2) the joint probability to characterize the relation between earthquake magnitude (m) and rupture location (s), $f_{M,S}(m,s)$; (3) the

probability of observing surface rupture (*sr*) conditioned on earthquake magnitude, $P(sr \neq 0|_m)$; (4) given a nonzero surface rupture the probability of observing a nonzero on-fault displacement at a site of dimension *z*, $P(D \neq 0|_{z,\ sr \neq 0})$ and (5) the probability of on-fault displacement exceeding a threshold D_0 conditioned on rupture geometry and earthquake size, $P(D \geq D_0|_{l/L,\ m,\ D \neq 0})$. The last conditional probability is lognormal and is developed from a predictive model that estimates on-fault displacements from empirical data. The annual exceedance rate of off-fault displacement $\gamma(d \geq d_0)$ is computed in a similar manner. The first three probabilities described for $\gamma(D \geq D_0)$ are also considered in $\gamma(d \geq d_0)$. In the computation of $\gamma(d \geq d_0)$, the probability of nonzero off-fault displacement given a nonzero surface rupture $[P(d \neq 0|_{r,\ z,\ sr \neq 0})]$ not only depends on the size of the site (*z*) but also on the perpendicular distance, *r*, between the site and the rupture. This is because the discontinuous off-fault displacements are expected to occur away from the fault due to a shears and fractures in the vicinity of principle rupture. The empirical GMPE to describe the probability of off-fault displacement exceeding a threshold d_0 $[P(d \geq d_0|_{r,\ m,\ d \neq 0})]$ is a function of *r* and *m* for $\gamma(d \geq d_0)$. The next paragraph explains the integration of these probabilities to MC-based permanent fault displacement hazard.

Our MC-based permanent fault displacement hazard assessment starts with the generation of synthetic earthquake catalogs to reflect the temporal seismic activity of a fault. The procedure for generating synthetic catalogs is the same as described in Section 2.2: each synthetic catalog contains a series of events that follows the designated magnitude recurrence model within the predefined catalog period. For each event in the synthetic catalog, Fig. 3.2 shows the proposed procedure to generate probabilistic on-fault and off-fault displacements at the sites (cells) covered by the region of interest. The grid size of sites (cells) is *z* (varying from 25 m to 200 m in Petersen et al., 2011 to account for different levels of accuracy in rupture probability) and mesh gridding is done within several hundred meters (e.g., 150 m) from each side of the fault because fault displacements decay rapidly with increasing distance from the ruptured fault segment. Thus, we do not generate grids for the entire region as in the case of MC-based MSRFs implemented for dynamic GMIMs.

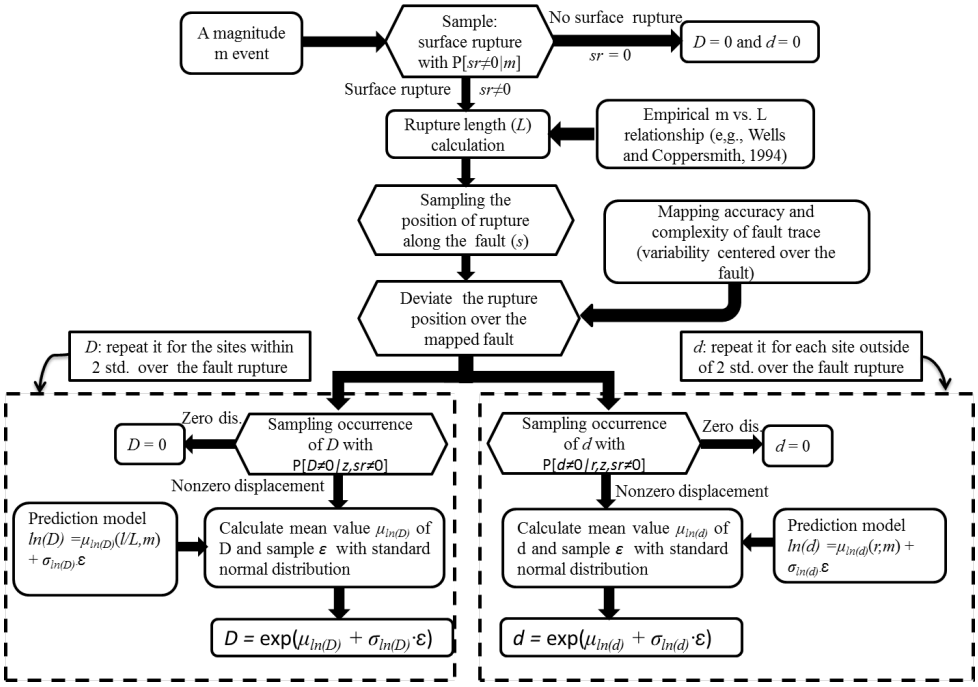

Fig. 3.2 Proposed MC-based permanent fault displacement hazard assessment procedure

We first compute the conditional probability of observing surface rupture on the fault, $P(sr \neq 0|_m)$, for each scenario event with a designated magnitude m in the earthquake catalog (Eq. (3.1)).

$$P\left(sr \neq 0\big|_m\right) = \frac{e^{(-12.51+2.053m)}}{1+e^{(-12.51+2.053m)}} \tag{3.1}$$

The conditional probability follows Bernoulli distribution that samples the "success" ($sr \neq 0$) or "failure" ($sr = 0$) of a random event under the computed probability given in Eq. (3.1). If Bernoulli distribution samples "failure", both on- and off-fault displacements are zero for that scenario event. If the earthquake with surface rupture is sampled, an empirical m vs. L scaling relationship is used (e.g., Wells and Coppersmith, 1994) to determine the rupture length, L. Note that in the context of extreme events, L can be greater than in standard hazard models due to cascading effects. A new L distribution for strike-slip earthquakes in the Anatolian Peninsula is given by Mignan et al. (2015) (see also STREST D3.5 report). The rupture position (s) is randomly placed along the entire fault assuming a uniform distribution. The likely deviation in the rupture location from the mapped fault trace due to mapping uncertainty and fault complexity is determined from a two-sided normal probability distribution proposed by Petersen et al. (2011) (see Tables 2 and 3 in the referred article). After determining the final location of the ruptured segment, the on- and off-fault displacements are generated as given in the dashed boxes in Fig. 3.2. The random generation of on- and off-fault displacements start with the consideration of probabilities $P(D \neq 0|_{z,\, sr \neq 0})$ and $P(d \neq 0|_{r,\, z,\, sr \neq 0})$. These probabilities are expressed as power functions and are given in a tabular format in Petersen et al. (2011) for different grid sizes. They also follow Bernoulli distribution and if the Bernoulli distribution samples "failure" for any one of these probabilities, the corresponding fault displacement is taken as zero. (In practice, $P(D \neq 0|_{z,\, sr \neq 0})$ can be taken as unity and Bernoulli distribution samples "success" whenever a non-zero surface rupture is generated). Otherwise, the on and off-fault displacements are estimated from the proposed empirical GMPEs by Petersen et al. (2011). The generic forms of these GMPEs are given in Eq. (3.2) and Eq. (3.3).

$$\ln(D) = \mu_{ln(D)}(l/L, m) + \varepsilon\sigma_{ln(D)}) \tag{3.2}$$

$$\ln(d) = \mu_{ln(D)}(r, m) + \varepsilon\sigma_{ln(d)}) \tag{3.3}$$

$\mu_{ln(D)}$ and $\mu_{ln(d)}$ are the logarithmic mean estimates of on- and off-fault displacements, respectively. $\sigma_{ln(D)}$ and $\sigma_{ln(d)}$ describe the logarithmic standard deviations associated with the on- and off-fault displacement GMPEs, respectively. ε designates the number of standard deviations above or below the logarithmic mean estimates. Consistent with the conventional thinking in GMPEs, D and d are log-normal varieties whereas ε is normally distributed in the above expressions. Petersen et al. (2011) propose three alternative predictive equations to estimate on-fault displacements depending on the observed data from past strike-slip earthquakes. These equations are strictly valid for on-fault sites (cells) after considering the mapping uncertainty and fault complexity while determining the location of ruptured segment on the principal fault. The off-fault displacement predictive model is used at the sites (cells) encircling the major ruptured fault segment. The off-fault sites are only within few hundred

meters from both sides of the ruptured fault segment due to rapid decay of fault displacements with distance.

The procedure given in Fig. 3.2 is repeated for all the earthquakes in the generated synthetic catalogs to compute the on- and off-fault displacement distributions at each cell (site). The annual exceedance rates of on-fault and off-fault displacements at each cell for predefined threshold levels are determined from the following expressions that are similar to Eq.(2.14).

$$\lambda_j(D \geq D_0) = \frac{total\ number\ of\ D \geq D_0\ at\ site\ j}{total\ number\ of\ simulated\ earthquake\ catalogs \times\ catalog\ period} \tag{3.4}$$

$$\lambda_j(d \geq d_0) = \frac{total\ number\ of\ d \geq d_0\ at\ site\ j}{total\ number\ of\ simulated\ earthquake\ catalogs \times\ catalog\ period} \tag{3.5}$$

In Eq. (3.4) and Eq. (3.5) *j* refers to the cell index whereas D_0 and d_0 are the threshold on-fault and off-fault displacements, respectively. The on-fault and off-fault displacement hazard curves at cell *j* are obtained from the computation of $\lambda_j(D \geq D_0)$ and $\lambda_j(d \geq d_0)$ for a set of D_0 and d_0, respectively. The total permanent displacement hazard curve at cell *j* is the sum of on- and off-fault hazard curves corresponding to cell *j*.

4 Parametric studies

We present several parametric case studies to show the implementation and implications of the theory discussed in this report. The case studies intend to emphasize the flexibility and robustness of MC-based simulations for probabilistic hazard assessment of dynamic GMIMs and permanent fault displacement. The presented results are important for the probabilistic risk assessment of geographically distributed and extended structures. We developed our own software, mainly Matlab^{TM} subroutines for running the case studies. Our software package was validated by comparisons with OpenQuake (Pagani et al., 2014) and crosscheck validation with the original journal papers (by contacting their authors).

he details of parametric case studies are given in the following subsections. The seismic sources are represented as fault segments in the case studies although they could also be chosen as area sources with some modifications in the procedures discussed in Section 2. The use of area sources would prevent addressing the near-fault effects on dynamic GMIMs.

4.1 PARAMETRIC STUDIES CONCERNING DYNAMIC GMIMS

Fig. 4.1 shows the results of the validation example of our codes for a fictitious 90^{o} dipping strike-slip fault segment of length 85 km. We consider pure-characteristic earthquake recurrence model with characteristic magnitudes ranging between Mw 7 and Mw 7.5. The annual slip rate is 15 mm/year for the fictitious fault. We ran 10000 simulations with a 100-year catalog period (total catalog period is 1,000,000 years) to obtain reliable hazard results for mean annual exceedance rates of about 10^{-4} (Musson, 2000). We used Akkar et al. (2014a; 2014b) GMPE to characterize the ground-motion amplitudes in the hazard analyses. The same fictitious scenario is modeled in OpenQuake in a conventional manner and the PGA hazard curves at the randomly selected rock sites (see upper right corner in Fig. 4.1 for the relative locations of sites with respect to the fault) are compared. The results computed by our codes agree well with OpenQuake for mean annual exceedance rates up to 10^{-4}. We repeated similar verification studies for different dynamic GMIMs and sites with locations different than those given in this exercise. These comparisons advocate the reliability of our codes to discuss how different levels of complexity (directivity, spatial correlation, conditional hazard etc.) are treated by MC-based approaches for probabilistic hazard assessment.

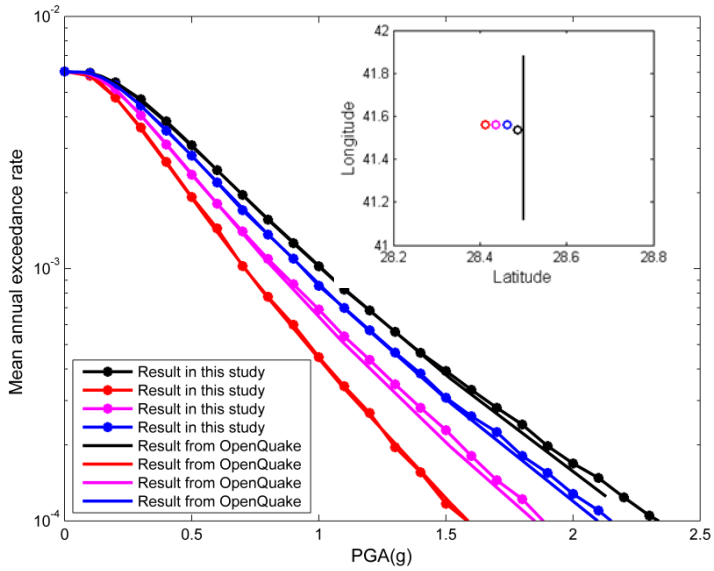

Fig. 4.1 Comparisons of OpenQuake PGA hazard curves with those computed from in-house Matlab™ codes for their validation for MC-based MSRFs technique. Note that this example disregards spatial correlation; near-fault directivity etc. as such complex models are not implemented in OpenQuake for conventional probabilistic hazard assessment

Similar to the above validation example, the following parametric case studies use a 90° dipping strike-slip fault although our codes can run hazard analyses for other faulting types. The fault length is 85 km and its seismogenic depth is taken as 15 km. The fictitious fault is assumed to have a slip rate of 15 mm/year producing characteristic earthquakes of M_w 7.0 to M_w 7.5. In all case studies, we used a 100-year catalog period and ran 10,000 simulations that results in a total catalog interval of 1,000,000 years. The spatial correlation model of Jayaram and Baker (2009) is used for the interdependency of dynamic GMIMs at closely spaced sites. The Akkar et al. (2014a; 2014b) GMPE and the Akkar et al. (2014c; 2014d) cross-correlation coefficients are used for ground-motion characterization and conditional hazard computations, respectively. These two studies use the same strong-motion database to develop the ground-motion predictive model and the correlations between the spectral ordinates. The site condition is fixed in all case studies and is represented by V_{S30} = 720 m/s. The size of coarse cells is chosen as 0.1°×0.1° and they are refined by 4×4 fine scale cells at sites closer to the fault.

Fig. 4.2 shows the influence of near-fault directivity effects on the distribution of 475-year return period spectral acceleration at T = 3.0s [S_a(3s)]. Fig. 4.2.a displays the distribution of S_a(3s) along the fine and coarse cells when the near-fault directivity effects are disregarded in the hazard assessment. The spectral amplitude distribution follows a uniform pattern making maximum in the vicinity of entire fault length and decreasing gradually towards distant sites from the fault. The spectral amplitude distribution in Fig. 4.2.b considers the directivity effects for the same case. The maximum spectral amplitudes are observed at the ends of the fault segment. They are approximately 20% to 25% larger with respect to those computed by disregarding the forward directivity. The spectral amplitudes in the middle portion of the fault segment are smaller in Fig. 4.2.b when compared to the corresponding spectral values in Fig. 4.2.a. These observations emphasize the importance of site location

with respect to fault orientation when near-fault effects are mapped on to hazard. The spectral amplitude comparisons between Fig. 4.2.a and Fig. 4.2.b suggest the insignificance of directivity effects for distances greater than 10 km from the fault strike. We note that these observations are confined to a specific source configuration and return period (i.e., 475-year return period). The influence of forward directivity on spectral amplitudes increases for larger return periods and higher seismic activity (i.e., larger slip rates).

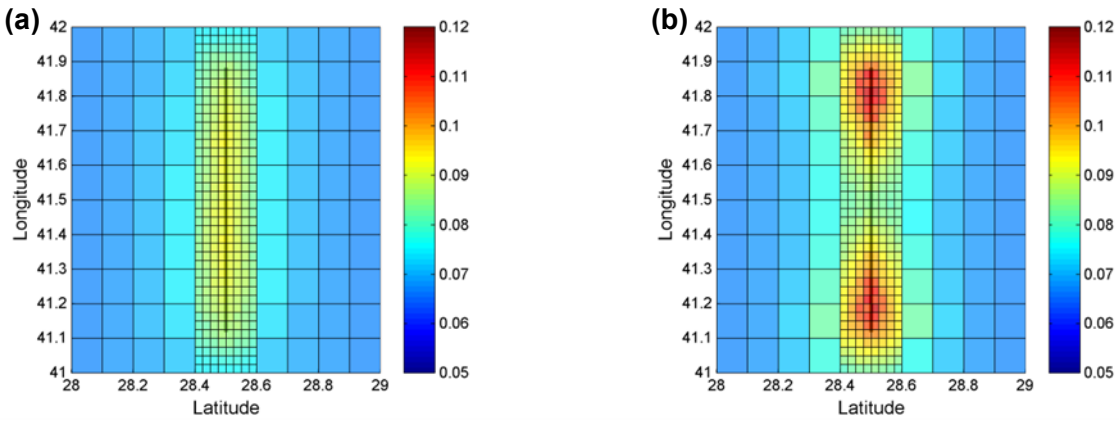

Fig. 4.2 Distribution of S_a(3s) amplitudes for 475-year return period without (a) and with (b) near-fault directivity effects

The left and right panels in Fig. 4.3 display the significance of conditional hazard on dynamic GMIMs and how it is accounted for by MC-based MSRFs approach. The plots show the distributions of S_a(1.0s) (Fig. 4.3a) and S_a(1.0)|S_a(3s) (Fig. 4.3.b) for 475-year return period. The distribution of S_a(1.0s) conditioned on S_a(3.0s) displays 10% to 15% lower spectral amplitudes with respect to the distribution of S_a(1.0s) at sites closer to the fault. Such spectral differences can be of importance for design or performance assessment of high-rise buildings under the influence of higher mode effects. For example, S_a(1.0s)|S_a(3.0s) distribution could be important for a tall building of 3.0s fundamental period (T_1) whose second mode (T_2 = 1.0s) affects its dynamic response significantly. To this end, the approach presented in this article would yield first-hand useful information for the regional variation of such vector GMIMs for regional probabilistic risk and loss assessment of building inventories (e.g., Weatherill et al. 2015).

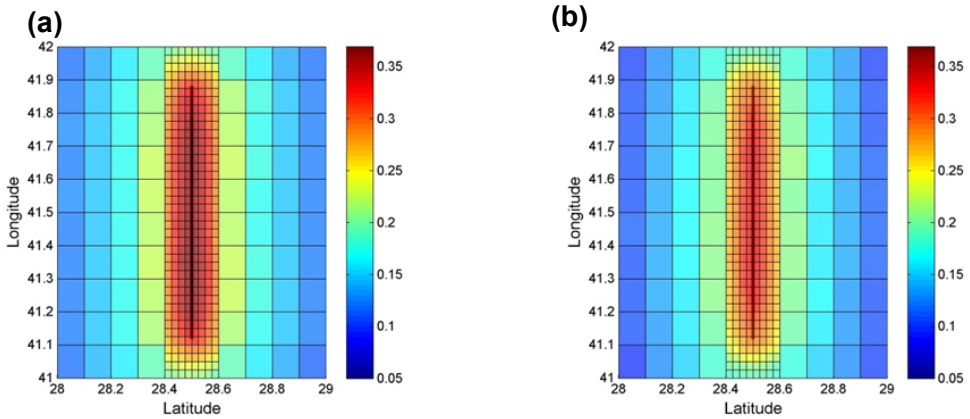

Fig. 4.3 Distribution of (a) Sa(1.0s) and Sa(1.0s)|Sa(3.0s) for 475-year return period

Fig. 4.4 illustrates a more complicated case study in which the significance of spatial correlation (SC) and near-fault forward directivity (NF) effects is discussed for three spectral periods at three different locations relative to the fault segment (Fig. 4.4.a). We consider a pair of sites at each location for spatial correlation effects. The pairs are closely spaced at locations 2 and 3 whereas the separation distance between the sites at location 1 is significantly large. The chosen spectral ordinates represent very short-period (PGA-T = 0.0s; Fig. 4.4.b), intermediate-period (T = 0.5s; Fig. 4.4.c) and long-period (T = 3.0s; Fig. 4.4.d) ground-motion demands. The comparative plots in Fig. 4.4 immediately suggest that consideration of spatial correlation has negligible influence at location 1 due to large separation distance between the sites. This observation particularly holds for very short period (Fig. 4.4.b) and intermediate period (Fig. 4.4.c) spectral ordinates. For longer periods (Fig. 4.4.d), disregarding SC effects at location 1 yields slightly lower spectral amplitudes with respect to the case when this effect is taken into consideration. We note that the insignificance of NF effects for PGA as well as Sa(0.5s) is location free (i.e. valid for all sites) because the forward directivity effects become considerable after T = 0.6s in the Shahi and Baker (2011) model. Disregarding spatial correlation has more pronounced effects for the 2nd and 3rd locations as the sites are closely spaced at these locations. Seismic hazard assessment that overlooks SC always underestimates spectral amplitudes and the underestimation increases with increasing annual exceedance rate and spectral period. The consideration of NF effects has different implications for the three locations considered in this report when periods shift to longer spectral period bands (Fig. 4.4.c). The NF effects are immaterial at the first location as it is far from the fault segment (~ 25 km). Consideration of NF effects amplifies Sa(3.0s) at location 3 and de-amplifies the same spectral ordinate at location 2. As discussed in Fig. 4.2, the near-fault forward directivity effects are pronounced at the ends of the fault segments (e.g., location 3) and become minimum at the middle part of the fault (e.g., location 2) that results in de-amplification of spectral ordinates.

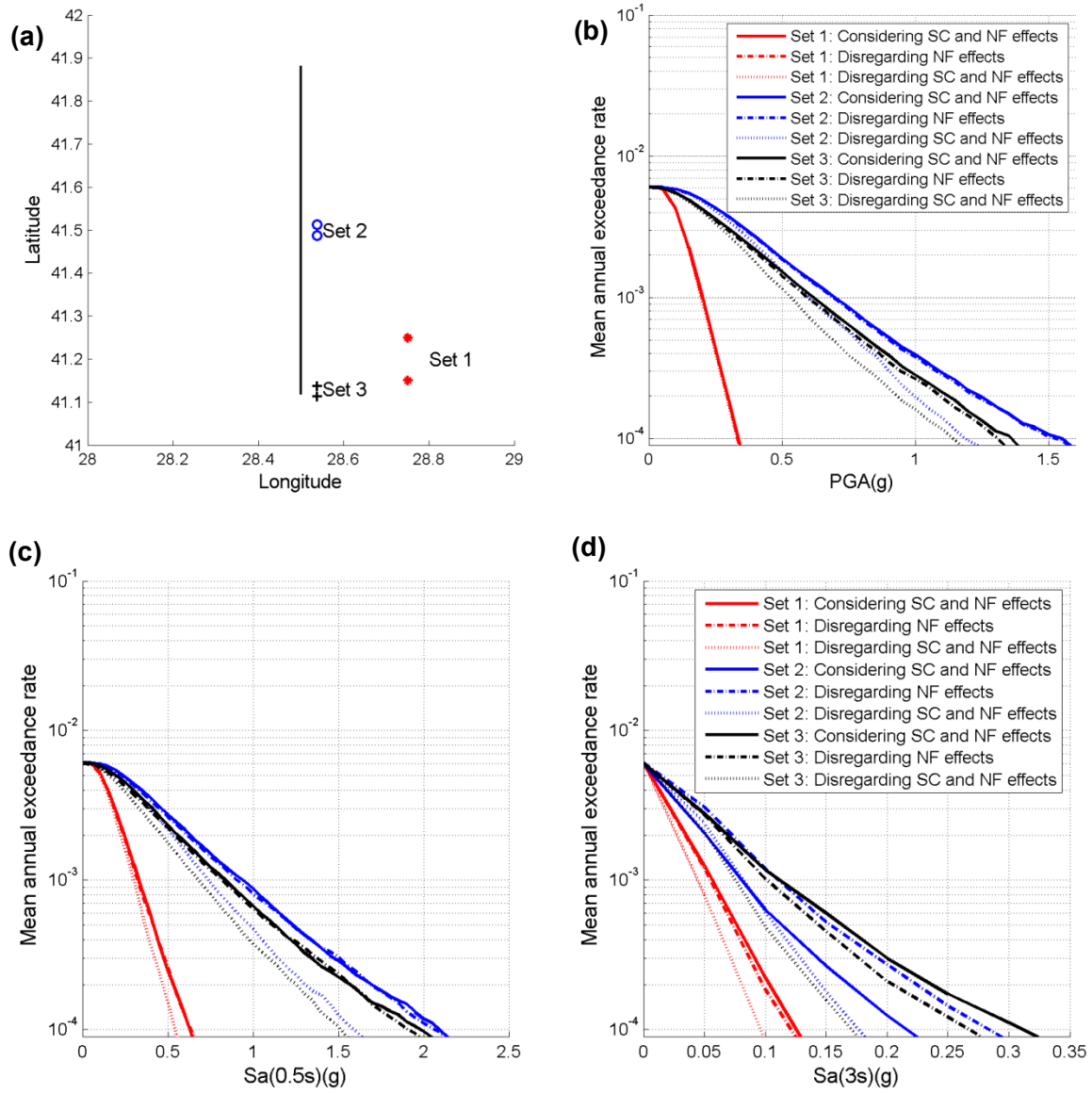

Fig. 4.4 Effect of spatial correlation (SC) and near-fault forward directivity (NF) effects at three different locations for three spectral periods (a) Plan-view of locations, sites and the fault segment, (b) joint hazard curves for PGA, (c) joint hazard curves for Sa(0.5s) and (d) joint hazard curves for Sa(3s)

4.2 PARAMETRIC STUDIES CONCERNING PERMANENT FAULT DISPLACEMENT

As in the previous section, our first example validates our Matlab™ codes for probabilistic permanent fault displacement hazard assessment. We duplicated the case study in Petersen et al. (2011) to validate our codes on MC-based probabilistic fault displacement hazard assessment. The case study in Petersen et al. (2011) assumes a strike-slip fault with a characteristic magnitude of M_w 7 occurring, on average, every 140 years. The authors assume nonzero permanent fault displacement whenever there is a surface rupture on the fault [i.e., $P(D \neq 0|_{z,\, sr \neq 0}) = 1$]. They also adopt accurately mapped fault trace scenario in their

example. We used the same assumptions and ran the probabilistic fault displacement hazard by generating 40,000 simulations with a catalog period of 100-year. We considered a stripe of 150m from both sides of the fault segment and computed the variation of permanent ground displacement along the entire fault length at every 100m. The sizes of sites on both sides of the fault segment are taken as 25m × 25m. The variation of permanent fault displacement is computed at every 1m within the 150m-stripe on both sides of the fault. Fig. 4.5.a shows the distribution of permanent fault displacement along the fault trace for a 475-year return period. The permanent fault displacements are maximum on the ruptured fault trace and attenuates very rapidly as one moves away from the fault in the perpendicular direction. Fig. 4.5.b compares the MC-based probabilistic permanent on-fault displacement at the center of the fault with the results of Petersen et al. (2011). The variation in the displacement profile is given along the 150m stripe from both sides of the fault. Our MC-based probabilistic approach yields very similar permanent displacement results to those computed from Petersen et al. (2011).

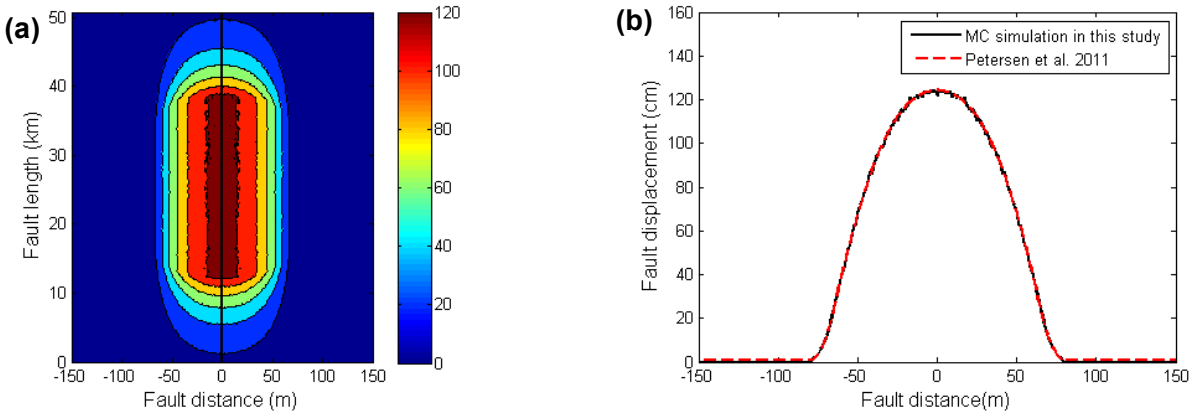

Fig. 4.5 Validation of MC-based probabilistic permanent fault displacement method by using the case study in Petersen et al. (2011): (a) distribution of 475-year permanent fault displacement along the fault strike, (b) comparison of computed 475-year on-fault displacement at the center of the fault with Petersen et al. (2011)

The seismic hazard level for designing pipelines usually depends on the importance of the pipelines and the consequences of their failure (e.g., IITK-GSDMA, 2007; ALA, 2005). Table 4.1 gives the classification of buried pipelines according to their importance and corresponding return periods to describe the seismic hazard levels described for their design (IITK-GSDMA, 2007). The listed target return periods (hazard levels) in Table 4.1 disregard the uncertainty in crossing angle and crossing location of pipelines at the fault segment. These factors can be important while designing or assessing the performance of continuous pipelines. For example, there are about 42 fault zones along the route of the Baku-Tbilisi-Ceyhan (BTC) pipeline and among these, five are identified as active, namely; Erzurum Fault (east and west) (close to the Georgian border) with 60 and 70 degrees of crossing angles, North Anatolian Fault (NAF) in midway between the border with 30 degrees of crossing angle and Çokak Fault (near Ceyhan) with 90 degrees of crossing angles. The uncertainty in the location accuracy of mapped fault is related to the uncertainty involved in pipeline crossing. It is an important factor for the probabilistic performance assessment of pipeline systems as, for example, some of the aforementioned faults along the BTC pipeline route have narrow features with only a few individual splay occurring zones of more than 10m but some of the other faults have complex formations with multiple fault splays (e.g.,

Erzurum, NAF and Cokak faults). The increase in the splay width is characterized by multiple fault planes (related to mapping accuracy) each of which will accommodate displacement during a seismic event. This fact would directly inflate the uncertainty in pipeline crossing. Thus, the permanent fault displacements to calculate the pipeline thickness to accommodate large relative movements that develop axial strains within the pipe cross-section should realistically account for the possible uncertainties in fault crossing angle and crossing location.

Table 4.1 Recommended design levels of seismic hazard

Pipe class	Probability of exceedance in 50 years	Return period (Years)
I	2%	2475
II	5%	975
III	10%	475
IV	No seismic design consideration required	

The depicted return periods in Table 4.1 provide indicatives for design level ground-motion amplitudes although some of our concerns about these hazard levels are already addressed in the previous paragraph. Moreover the performance and design of critical lifelines such as continuous pipelines require the consideration of low-probability-high-consequence events that are generally referred to as "*perfect storm"* and "*black swan"* in risk analysis. Consideration of such rare events (e.g., extreme cascading ruptures by adding knowledge from the physics of rupture propagation by dynamic stress; Mignan et al., 2015) would let the owner evaluate the performance of the structural system under critical circumstances. The term *"perfect storm"* refers to an event resulting in a conjunction of rare but known events (Pate-Cornell, 2012). It involves aleatory variability, which is inherent in a random phenomenon. The *"black swan"* events represent the ultimate epistemic uncertainty due to lack of fundamental knowledge, where the distribution of a parameter is unknown or even the existence of the phenomenon itself is also unknown (Pate-Cornell, 2012). The current probability-based seismic risk assessment considers the occurrence likelihoods of events and the resulting consequences. The "black swan" events are not foreseeable from usual statistical considerations such as correlations, regressions, standard deviations and return periods. Bayesian probability is one way of quantifying the risk for extremely rare events. A good example for very rare events is the 2011 Tohoku, Japan earthquake that produced tsunami waves of 14m in the Northeast of Japan. The unexpected tsunami waves caused nuclear meltdown in the Fukushima Daiichi nuclear power plant that was designed for a maximum wave height of 5.7m [corresponds to the exceedance rate of which is less than 1% in 50 years (INPO, 2011)]. The Fukushima earthquake can be a good example for a *"perfect storm"* case.

Under the light of above discussions, the next parametric study shows how the location uncertainty in pipe crossings along the fault affect the design and performance assessment of continuous pipelines subjected to permanent fault displacement. The axial strains (tensile or compression) developed in the pipeline due to fault rupture emerging at the surface result in various failure modes (e.g., pipe rupture or buckling) at the segments crossing the fault. The nature and level of stress concentrations at such critical pipe segments depend on the dominant component of fault displacement (normal, reverse, left-lateral or right-lateral slip),

pipeline orientation, location of pipe crossing along the fault segment, burial depth, soil or backfill material properties, coating, pipe material and geometric properties (steel grade, diameter and thickness). As already indicated we will only consider the location uncertainty of pipe crossing in this parametric example. We assume that the pipe is steel with a diameter of D = 850mm and a thickness of t = 21mm. These properties are taken from the BTC pipeline segment crossing the Çokak fault segment. The pipeline crosses the Çokak Fault with an angle of 90°. We also assume that the that the backfill material is soft to medium sand and the pipe yields in compression or tension, and the effects of local buckling is ignored. We used a simplified pipe-soil interaction model to compute the axial strains and corresponding displacement demands at the onset of critical limit states that are discussed in the following paragraph for this parametric study.

Fig. 4.6.a shows a pipeline-fault (strike-slip) configuration to quantify the variation of deformation demands on the pipeline segment for different crossing angles (α) and pipe crossing locations along the fault trace (designated by *x* measured from the left end of the representative configuration). The annual exceedance rates corresponding to the permanent fault displacements of 70cm, 250cm and 350cm are computed for $0 \le x \le L$ after running 40,000 MC simulations for a 100-year catalog period (i.e., 4,000,000 years of total catalog duration). The imposed permanent ground displacements grossly represent tensile strains developed on the butt-welded continuous pipelines for onset of yielding (70cm) ,10% probability of tensile rupture (250cm), and 90% probability of tensile rupture (350cm) when pipeline is perpendicular to the fault (i.e., $\alpha = 90°$). The former performance level represents the normal operability (pipeline serviceability under frequent events) whereas the second displacement limit is used for pressure integrity: an important condition to be satisfied under design level ground motions. The last displacement limit (350cm) is assumed to mimic a "perfect storm" event and accounts for the aleatory variability due to nature of seismic events that can be involved during the economic life of the pipeline. The mean annual exceedance rates as a function of pipe crossing location (i.e., *x*) along the fault segment are given in Fig. 4.6.b for a fault model rupturing with characteristic magnitudes between M_w 7 and M_w 7.5 with an average slip rate of 2 cm/year. These parameters may characterize the seismicity in Çokak Fault. Fig. 4.6.b depicts the sensitivity of annual exceedance rates to the location of pipe crossing. Given any one of the performance levels, the mean annual exceedance rates are very low for pipe crossing locations close to the ends of the fault segment. The exceedance rates are significantly high towards the center of the fault segment. In essence, the permanent fault displacements for the designated pipe performance levels will be the result of very rare events for continuous pipelines crossing the fault segments closer to their edges. The same plots suggest that relatively more frequent earthquakes should be of concern for performance evaluation of continuous pipelines when their fault crossings are more likely to occur at the middle portion of the fault segments. Currently, the seismic design of continuous pipelines is based on fixed mean annual exceedance rates (e.g., IITK-GSDMA 2007; ALA 2005) that seem to yield a non-uniform risk and loss assessment for their performance verification. Note that the axial strain in the pipe depends on the pipe-fault orientation angle (pipe crossing angle) as well as the properties of the fault, pipe and soil. As these parameters would vary from on segment to the other, the return periods corresponding to these limit states will also change in turn. Therefore, the results presented herein should be considered preliminary and generic.

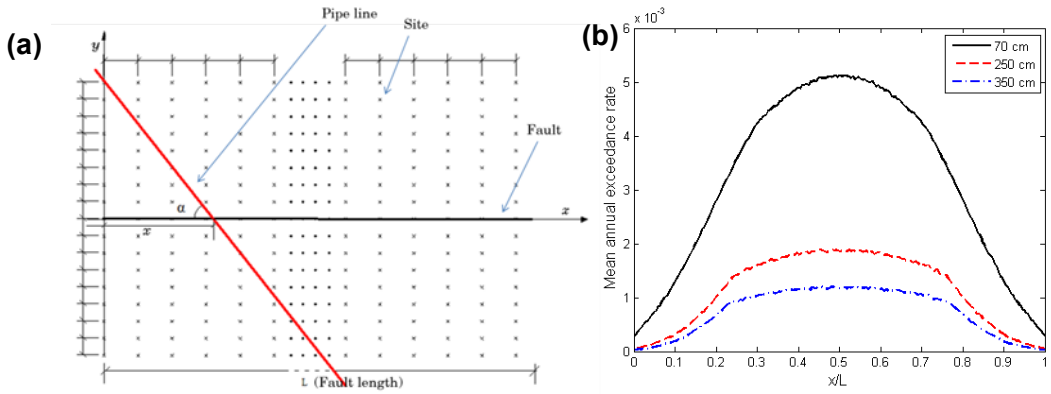

Fig. 4.6 (a) Fault, pipeline and site lay out: x denotes the pipe crossing location along the fault, α is the crossing angle between the pipeline and fault, L is the fault length; (b) Mean annual exceedance rates as a function of pipe crossing location for permanent ground displacement of 70cm, 250cm and 350cm. (α = 90° in the given example)

5 Conclusion

We present the implementation of MC-based simulation techniques for probabilistic hazard assessment of dynamic GMIMs and permanent fault displacement that are of significance for the hazard assessment of geographically distributed and extended structures for low-probability-high-consequence seismic events. Determination of hazard levels for geographically distributed and geographically extended structures is the major objective of Deliverable 3.2 in the STREST project. The MC-based simulations are incorporated with the multi-scale random fields (MSRFs) approach to account for the spatial correlation, near-fault forward directivity and conditional hazard (cross-correlation) in the variation of dynamic intensity measures. The multi-scale random fields provide significant flexibility for instant modification of intra-event aleatory variability whenever it is necessary. Our probabilistic permanent fault displacement method considers the uncertainty in the pipeline crossing location and pipeline crossing angle. Our parametric studies show that these complicated seismological factors are important for a proper hazard assessment of geographically extended critical infrastructures. In particular, the location uncertainty in fault crossing can affect the annual exceedance rates at different performance levels (i.e., serviceability, design and "*perfect storm*" cases). This fact may affect the decisions on the probabilistic risk assessment of continuous pipelines. Consideration of all these factors via conventional (integral) PSHA can be computationally a challenging task. The MC-based techniques discussed in the report provide flexibility to reflect the effects of complicated seismological features on to hazard without running complicated probabilistic hazard integrals. Note that the discussions on the hazard assessment of continuous pipelines are preliminary and enriched by other parametric studies for more conclusive results during the course of the project.

References

Akkar, S., M. A. Sandikkaya, and J. J. Bommer. 2014a. Empirical ground-motion models for point-and extended-source crustal earthquake scenarios in Europe and the Middle East. *Bulletin of Earthquake Engineering* 12(1): 359–387.

Akkar, S., M. A. Sandikkaya, and J. J. Bommer. 2014b. Erratum to: Empirical ground-motion models for point- and extended-source crustal earthquake scenarios in Europe and the Middle East. *Bulletin of Earthquake Engineering* 12(1):389–390.

Akkar, S., M. A. Sandikkaya, and B. O. Ay. 2014c. Compatible ground-motion prediction equations for damping scaling factors and vertical-to-horizontal spectral amplitude ratios for the broader Europe region. *Bulletin of Earthquake Engineering* 12(1): 517-547.

Akkar, S., M. A. Sandikkaya, and B. O. Ay. 2014d. Erratum to: Compatible ground-motion prediction equations for damping scaling factors and vertical-to-horizontal spectral amplitude ratios for the broader Europe region. *Bulletin of Earthquake Engineering* 12(3): 1429-1430.

American Lifeline Alliance (ALA). 2005. *Design Guidelines for Seismic Resistant Water Pipeline Installations*. Report FEMA, NIBS and ALA 2005/03. G&E Engineering Systems Inc.

Assatourians, K., and G. M. Atkinson. 2013. EqHaz: An open-source probabilistic seismic-hazard code based on the Monte Carlo simulation approach. *Seismological Research Letters* 84(3): 516-524.

Atkinson G. M., and K. Goda. 2013. *Seismic risk analysis and management of civil infrastructure systems: an overview*, Chapter 1. Handbook of Seismic Risk Analysis and Management of Civil Infrastructure Systems. Cambridge, UK: Woodhead Publishing Ltd.

Baker, J., N. Jayaram. 2008. Correlation of Spectral Acceleration Values from NGA Ground Motion Models. *Earthquake Spectra* 24(1): 299–317.

Bayless, J., and P. Somerville. 2013. *Bayless-Somerville Directivity Model*. Report PEER 2013/09. Berkeley, Calif.: Pacific Earthquake Engineering Research Center, University of California.

Boore, D. M., J. F. Gibbs, W. B. Joyner, J. C. Tinsley, and D. J. Ponti. 2003. Estimated ground motion from the 1994 Northridge, California, earthquake at the site of the Interstate 10 and La Cienega Boulevard bridge collapse, West Los Angeles, California. *Bulletin of the Seismological Society of America* 93(6): 2737–2751.

Bradley, B. A. 2011. Empirical correlation of PGA, spectral accelerations and spectrum intensities from active shallow crustal earthquakes. *Earthquake Engineering and Structural Dynamics* 40(15):1707–1721.

Bradley, B. A. 2012a. Empirical correlations between cumulative absolute velocity and amplitude-based ground motion intensity measures. Earthquake Spectra 28(1): 17–35.

Bradley, B. A. 2012b. Empirical Correlations between Peak Ground Velocity and Spectrum-Based Intensity Measures. *Earthquake Spectra* 28(1): 37–54.

Chen, Q., A. Seifried, J. E. Andrade, and J. W. Baker. 2012. Characterization of random fields and their impact on the mechanics of geosystems at multiple scales. International *Journal for Numerical and Analytical Methods in Geomechanics* 36(2):140–165.

Chioccarelli, E., S. Esposito, and I. Iervolino. 2012. Implementing conditional hazard for earthquake engineering practice: the Italian example. *In Proceedings of the 15th World Conference on Earthquake Engineering,* Lisbon, Portugal.

Chiou, B. S. J., and P. Spudich. 2013. *The Chiou and Spudich Directivity Predictor DPP*. Report PEER 2013/09. Berkeley, Calif.: Pacific Earthquake Engineering Research Center, University of California.

Cimellaro, G. P. 2013. Correlation in spectral accelerations for earthquakes in Europe. *Earthquake Engineering & Structural Dynamics* 42(4): 623-633.

Cornell, C. A. 1968. Engineering seismic risk analysis. *Bulletin of the Seismological Society of America* 58(5): 1583-1606.

Crowley, H., and J. J. Bommer. 2006. Modelling seismic hazard in earthquake loss models with spatially distributed exposure. *Bulletin of Earthquake Engineering* 4(3): 249-273.

Esposito, S., and I. Iervolino. 2011. PGA and PGV spatial correlation models based on European multievent datasets. *Bulletin of the Seismological Society of America* 101(5): 2532–2541.

Goda, K. and G. M. Atkinson. 2009. Probabilistic characterization of spatially correlated response spectra for earthquakes in Japan. *Bulletin of the Seismological Society of America* 99(5): 3003-3020.

Goda, K., and H. P. Hong. 2008. Spatial Correlation of Peak Ground Motions and Response Spectra. *Bulletin of the Seismological Society of America*. 98(1): 354–365.

Iervolino, I., M. Giorgio, C. Galasso and G. Manfredi. 2010. Conditional hazard maps for secondary intensity measures. *Bulletin of the Seismological Society of America* 100(6): 3312–3319.

IITK-GSDMA. 2007. *Guidelines for seismic design of buried pipelines*. Kanpur, India: Indian Institute of Technology.

Institute of Nuclear Power Operations (INPO). 2011. *Special Report on the Nuclear Accident at the Fukushima Daiichi Nuclear Power Station.* Report INPO 2011/5, Atlanta, GA.

Jayaram, N., and J. W. Baker. 2009. Correlation model of spatially distributed ground motion intensities. *Earthquake Engineering & Structural Dynamics* 38(15): 1687–1708.

Loth, C., and J. W. Baker. 2013. A spatial cross-correlation model of spectral accelerations at multiple periods. *Earthquake Engineering & Structural Dynamics* 42(3): 397–417.

Mignan, A., L. Danciu and D. Giardini (2015), Reassessment of the maximum fault rupture length of strike-slip earthquakes and inference on M_{max} in the Anatolian Peninsula, Turkey, Seismol. Res. Lett., in press

Musson, R. M. W. 1999. Determination of design earthquakes in seismic hazard analysis through Monte Carlo simulation. *Journal of Earthquake Engineering* 3(4): 463-474.

Musson, R. M. W. 2000. The use of Monte Carlo simulations for seismic hazard assessment in the UK. *Annali Di Geofisica* 43(1): 1–9

Pate´-Cornell E. 2012. On ‘‘Black Swans’’ and ‘‘Perfect Storms’’: risk analysis and management when statistics are not enough. *Risk Analysis* 32:1823–1833.

Petersen, M. D., T. E. Dawson, R. Chen, T. Cao, C. J. Wills, D. P. Schwartz, and A. D. Frankel. 2011. Fault displacement hazard for strike-slip faults. *Bulletin of the Seismological Society of America* 101(2): 805–825.

Rowshandel, B. 2013. Rowshandel’s NGA-West2 directivity model. Report PEER Report 2013/09, Berkeley, Calif.: Pacific Earthquake Engineering Research Center, University of California.

Shahi, S., and J. W. Baker. 2011. An empirically calibrated framework for including the effects of near-fault directivity in probabilistic seismic hazard analysis. *Bulletin of the Seismological Society of America* 101(2): 742–755.

Sokolov, V., and F. Wenzel. 2011a. Influence of ground-motion correlation on probabilistic assessments of seismic hazard and loss: sensitivity analysis. *Bulletin of Earthquake Engineering* 9(5): 1339–1360.

Sokolov, V., and F. Wenzel. 2011b. Influence of spatial correlation of strong ground motion on uncertainty in earthquake loss estimation. *Earthquake Engineering & Structural Dynamics* 40(9): 993–1009.

Somerville, P. G. 2003. Magnitude scaling of the near fault rupture directivity pulse. *Phys. Earth Planet* 137(1) 201–212.

Stepp, J. C., I. Wong, J. Whitney, R. Quittmeyer, N. Abrahamson, G. Toro, R. Youngs, K. Coppersmith, J. Savy, T. Sullivan, and Yucca Mountain PSHA Project Members. 2001. Probabilistic seismic hazard analyses for ground motions and fault displacement at Yucca Mountain, Nevada. *Earthquake Spectra* 17(1): 113–150.

Taleb, N. N. 2007. *The Black Swan: The Impact of the Highly Improbable*. New York: Random House.

Tothong, P., C. A. Cornell, and J. W. Baker. 2007. Explicit-directivity-pulse inclusion in probabilistic seismic hazard analysis. *Earthquake Spectra* 23(4): 867–891.

Wang M., and T. Takada. 2005. Macrospatial Correlation Model of Seismic Ground Motions. *Earthquake Spectra* 21(4):1137–1156.

Weatherill, G. A., V. Silva, H. Crowley, and P. Bazzurro. 2015. Exploring the impact of spatial correlations and uncertainties for portfolio analysis in probabilistic seismic loss estimation. *Bulletin of Earthquake Engineering* 13 (4): 957-981.

Wells, D. L., and K. J. Coppersmith. 1994. New empirical relationships among magnitude, rupture length, rupture width, rupture area, and surface displacement. *Bulletin of the Seismological Society of America* 84(4): 974–1002.

Wesson, R. L., and D. M. Perkins. 2001. Spatial correlation of probabilistic earthquake ground motion and loss. *Bulletin of the Seismological Society of America* 91(6): 1498-1515.

Youngs, R. R., W. J. Arabasz, R. E. Anderson, A. R. Ramelli, J. P. Ake, D. B. Slemmons, J. P. McCalpin, D. I. Doser, C. J. Fridrich, F. H. Swan III, A. M. Rogers, J. C. Yount, L. W. Anderson, K. D. Smith, R. L. Bruhn, L. K. Knuepfer, R. B. Smith, C. M. dePolo, K. W. O'Leary, K. J. Coppersmith, S. K. Pezzopane, D. P. Schwartz, J. W. Whitney, S. S. Olig, and G. R. Toro. 2003. A methodology for probabilistic fault displacement hazard analysis (PFDHA*). Earthquake Spectra* 19(1): 191–219.